ACS APPLIED MATERIALS & INTERFACES

Research Article

www.acsami.org

# Growth of $Cu_2ZnSnS_4$ Nanocrystallites on $TiO_2$ Nanorod Arrays as Novel Extremely Thin Absorber Solar Cell Structure via the Successive-Ion-Layer-Adsorption-Reaction Method

Zhuoran Wang and George P. Demopoulos*

Materials Engineering, McGill University, 3610 University Street, Montreal, Quebec Canada H3A 0C5

Supporting Information

**ABSTRACT:** $Cu_2ZnSnS_4$ (CZTS) is an environmentally benign semiconductor with excellent optoelectronic properties that attracts a lot of interest in thin film photovoltaics. In departure from that conventional configuration, we fabricate and test a novel absorber-conductor structure featuring in situ successive-ion-layer-adsorption-reaction (SILAR)-deposited CZTS nanocrystallites as a light absorber on one-dimensional $TiO_2$ (rutile) nanorods as an electron conductor. The effectiveness of the nanoscale heterostructure in visible light harvesting and photoelectron generation is demonstrated with an initial short circuit current density of 3.22 mA/cm$^2$ and an internal quantum efficiency of ~60% at the blue light region, revealing great potential in developing CZTS extremely thin absorber (ETA) solar cells.

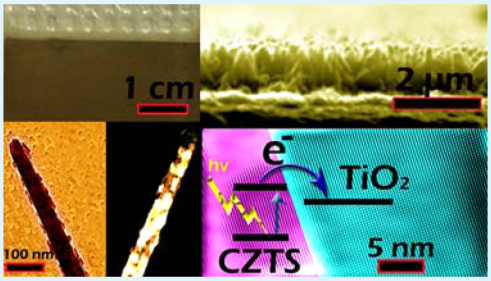


**KEYWORDS:** *$Cu_2ZnSnS_4$ nanocrystallites, $TiO_2$ nanorods, heterostructure, solution processing, ETA solar cells*

## INTRODUCTION

Visible light capturing and conversion to electricity or hydrogen (solar fuel) is a critical area of research in our efforts to develop alternative renewable energy solutions. As a semiconductor with an optimal bandgap for harvesting sunlight as well as its earth-abundant, environmentally benign compositional nature, $Cu_2ZnSnS_4$, or CZTS (in particular its kesterite polymorph), has been made the subject of major interest since the late 2000s as a highly promising candidate for solar cell applications.[1] Generally, to extract the generated photoelectrons from absorber materials, different charge-extraction strategies have been employed to design optoelectronic devices.[2] For CZTS, the most common strategy being used is the built-in electric field within a thin film p−n junction configuration.[3−5] However, for CZTS to function simultaneously as both light absorber and charge conductor, the film must be of high-purity and defect-free to enable high carrier mobility, requirements that seriously limit its further development in this regard. In the face of this limitation, it would be advantageous if CZTS could be only used for light harvesting while another wide bandgap semiconductor is used as charge conductor, i.e., creating an absorber-conductor configuration instead.

Absorber-conductor based devices, for example, dye-sensitized solar cells, rely on favorable energetic offset between the absorber LOMO and the photoanode conduction band to realize effective electron injection.[6] Though organic semiconductors like dye molecules,[7] polymers[8,9] and the current "hot" methylammonium lead halides perovskites[10,11] have seen impressive progress, the long-term stability issue still makes inorganic semiconductors more preferable as light absorbers. In this regard extremely thin absorber (ETA) solar cells featuring inorganic semiconductors like PbS, CdS, CdSe, $Sb_2S_3$,[12] etc. have been investigated for photon-electron conversion applications. However, nanocrystalline semiconductors consisting of less-toxic earth-abundant elements are preferable to elements like Pb, Cd, Sb, etc. In this regard it is noteworthy the results obtained with tin sulfide (SnS), an environmentally benign and simple in composition semiconductor, recorded 4% efficiency.[13] Other visible light sensitive semiconductors, for example, copper sulfide ($Cu_2S$), have shown potential in ETA solar cell applications.[14] However, the instability of SnS to oxygen or an acidic environment and the very high propensity to be degenerate of copper sulfides due to the coexistence of many possible phases with composition ranging from $CuS_2$ to $Cu_2S$ are responsible to the slow improvement of their device performance. In comparison, CZTS, due to its optimal theoretical band gap of 1.5 eV as well as its less-toxic earth-abundant nature, plus the high resistance to oxidation and acidic corrosion, having already been proven an excellent thin film photovoltaic solar cell material, could also be suited in this context as a light absorber only, while relying on another high-mobility component for charge transfer hence to relieve the issue of severe crystal defects in CZTS.

To date, only very few reports have explored this avenue, which is most likely due to the much more challenging synthesis of high grade quaternary CZTS than that of simple binary semiconductors. The concept of using CZTS as a sensitizer was first brought up by Wang et al.,[15] where

Received: June 26, 2015
Accepted: September 30, 2015
Published: September 30, 2015





DOI: 10.1021/acsami.5b05732
ACS Appl. Mater. Interfaces 2015, 7, 22888−22897

mesoporous $TiO_2$ electron conductor was sensitized by dipping into the ex-situ prepared CZTS nanopowder suspension. However, the CZTS particles failed to fill the pores of the $TiO_2$ mesoporous film residing on the surface instead of having as a consequence to lower the effective cross section for photoelectron generation, resulting in a very low photocurrent density. A similar device structure was also investigated by Dai et al.[16] and apparently again because of their similar powder suspension sensitizing procedure, lack of good contact between CZTS and $TiO_2$ rendered the device ineffective. Therefore, in situ deposition and growth of CZTS directly on the $TiO_2$ nanostructured mesoporous film should avoid this problem enabling functional photovoltaic devices to be developed.

In developing such inorganic sensitized ETA solar cell, the choice of $TiO_2$ nanostructure is equally critical as the conventional nanoparticle-based mesoporous film suffers from severe recombination losses.[17,18] By far vertically aligned single crystalline nanowires or nanorods because of their short electron pathway[19−21] can offer an advantageous conducting network in this regard. Ho et al. attempted recently to deposit CZTS via a chemical bath method on rutile nanorods but their deposits were not uniform and they had to resort to predeposition of a CdS adhesion layer.[22] Cadmium however is extremely toxic; moreover, a nanoscale study of the rutile/CZTS interface without the interference from the presence of CdS is a critical prerequisite in understanding and ultimately enabling the development of extremely thin absorbing CZTS-based solar cells.

With the view of overcoming the limitations of previous efforts in preparing TNR@CZTS nanostructures in an extremely thin absorbing solar cell configuration, we have developed and presented a SILAR-based approach that allows for better light absorber penetration. To this end we employ a three-step successive ionic layer adsorption and reaction (SILAR) method followed by high temperature annealing to control the in situ deposition and growth of CZTS nanocrystallites on rutile $TiO_2$ nanorod arrays (TNR@CZTS) that are subjected to nanoscale characterization and early stage optoelectronic performance evaluation and optimization. The newly configured TNR@CZTS heterostructure is successfully demonstrated to be effective in visible light-driven photoelectron generation, revealing a great potential for devising all-inorganic stable and green PV devices.

## EXPERIMENTAL SECTION

**Material Synthesis.** As shown in Figure S1, in the first step, in order to grow vertically aligned $TiO_2$ nanorods, a piece of precleaned fluorine doped tin oxide (FTO) glass (Sigma-Aldrich, 7 Ω/sq) was placed with the conductive side facing downward in a 125 mL Teflon container. An acidic solution was added by mixing 10 mL of DI water, 10 mL of concentrated hydrochloric acid solution (36.5% by weight, Fisher Scientific), and 1 mL of titanium butoxide (97%, Sigma-Aldrich). The whole container was then placed into a stainless steel autoclave and kept at 150 °C for 2 h. After the hydrothermal reaction, well aligned $TiO_2$ nanorod arrays had been deposited on the FTO glass that were subsequently subjected to thermal treatment-annealing at 450 °C in air.

To deposit the CZTS precursor material containing Cu, Zn, Sn, and S on the $TiO_2$ nanorod array, three successive-ion-layer-adsorption-reaction (SILAR) steps were applied. For the first SILAR step (SILAR 1), 100 mL of 0.02 M $CuCl_2$ (99%, Alfa Aesar) and 0.16 M $Na_2S$ (98%, Sigma-Aldrich) aqueous solution was prepared separately in two containers. Then the as-prepared $TiO_2$ film on FTO glass was immersed into $CuCl_2$ aqueous solution and $Na_2S$ aqueous solution successively with a 1 min interval time. This process was repeated for 10 times and the color of the sample was observed to change from white to light green. The second SILAR step (SILAR 2) was similar to the difference that instead of $Cu^{2+}$, 0.02 M $SnCl_2$ (98%, Sigma-Aldrich) and 0.16 M $Na_2S$ aqueous solutions were prepared in which the film from SILAR step 1 was alternatively dipped in and out 10 times. The obtained film was slightly reddish after SILAR 2. To complete the precursor preparation, the last SILAR step was performed using 0.1 M $ZnCl_2$ (99.99%, Sigma-Aldrich) aqueous solution as the cationic ion provider with the same $Na_2S$ solution and the sequential dipping was repeated 5 times. Via this three SILAR step sequence, all four CZTS elements were successfully deposited on the $TiO_2$ nanorod array film. After that, the film was subjected to annealing at 500 °C for 1 h in the tube furnace in the presence of 0.1 g of elemental sulfur at inert atmosphere to prevent decomposition of CZTS during annealing. The color of the annealed film changed from light green to light brown. To effect the removal of any excess ZnS as well any incompletely reacted $Cu_yS/SnS_x$ impurity phases, the films were also subjected to further treatment by immersion in strong HCl acid (4 M).

**Characterization Methods.** Thermo Scientific K-Alpha X-ray photoelectron spectroscopy (XPS) was used for chemical state and element depth profile analysis. For the depth profile, etching was performed using Ar ion gun sputtering at 3 keV and high current to achieve a maximum etching rate. A Hitachi SU3500 scanning electron microscope (SEM) was used for morphology investigation. Raman spectroscopy was performed using a Renishaw inVia Raman spectrometer equipped with a LEICA optical microscope. A near-infrared laser (785 nm) was used as the excitation source. Transmission electron microscopes (FEI Tecnai G2 F20 200 kV Cryo-STEM equipped with EDAX Octane T Ultra W/Apollo XLT2 SDD and TEAM EDS Analysis System) were used for nanostructure investigation. Inductively coupled plasma-optical emission spectrometry (ICP-OES) was applied to determine the metallic elemental ratio of CZTS. An IPCE/EQE system from PVM Inc. was used for optical and external quantum efficiency measurements. The Newport AM1.5 solar simulator was used for $J-V$ characteristic measurement.

## RESULTS AND DISCUSSION

The preparation of the TNR@CZTS nanostructure includes three main steps as described by the schematic in Figure S1: (1) growth of $TiO_2$ nanorod arrays (TNR) on FTO glass; (2) deposition of CZTS precursor containing copper, zinc, tin, and sulfur elements onto the TNR film, in this step, the successive ionic layer adsorption and reaction (SILAR) method was used to ensure a uniform CZTS precursor deposit composition on each nanorod; (3) annealing to induce formation of crystalline CZTS on TNR.

After the completion of TNR@CZTS nanostructure construction, scanning electron microscopy (SEM) was applied to study the morphology of the final product. Figure 1a,c shows the cross-sectional SEM images of the $TiO_2$ nanorod arrays before (upper) and after (lower) CZTS deposition, where the insets depict the higher magnification image of the marked area. The near-vertically aligned hydrothermally grown $TiO_2$ nanorods are clearly seen,[6,19] In addition, the top view image in Figure 1b,d helps to verify the vertically grown nanostructure and confirm its uniformity to a certain extent. From the inset digital photographs, the clear color darkening signifies the formation of visible light absorbing material on the final product; however, no significant microstructure differences could be seen under this resolution; this means that the $TiO_2$ morphology has been well preserved following its exposure to the harsh chemical and thermal steps involved with CZTS deposition; the deposition of the latter CZTS crystallites was positively identified with further characterization.


DOI: 10.1021/acsami.5b05732
ACS Appl. Mater. Interfaces 2015, 7, 22888−22897

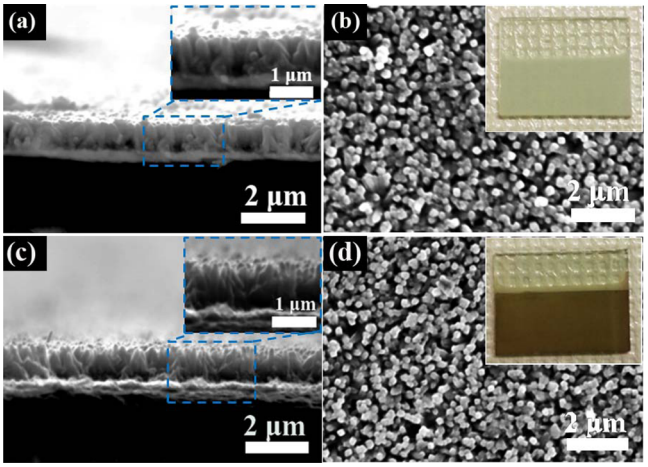


**Figure 1.** (a) Cross-section and b) top view SEM images of the $TiO_2$ nanorod arrays on FTO glass; (c) cross-section and (d) top view SEM images after CZTS deposition. The insets of parts b and d show digital photographs of the TNR on FTO glass before and after CZTS deposition, respectively.

In order to prove the presence of all elements in TNR@CZTS, X-ray photoelectron spectroscopy (XPS) was applied. Figure S2 shows the high-resolution XPS spectra. The clearly distinguishable peaks of Cu, Zn, Sn, and S as well as Ti and O confirm the validity of our initial nanostructure design. After employing the 3 keV Ar ion gun to etch the surface for 1 min and in situ capturing of new spectra (Figure S3), the signals of Cu, Zn, and Sn are seen to become weaker but still to show up as distinct peaks. However, the spatial distribution of elements still remains unclear. Hence we kept using Ar ion gun to etch through the entire film and the overall depth profile obtained is shown in Figure 2a, where the boundaries between the target layer, presumably TNR@CZTS film (green region), FTO layer (pink region), and glass substrate (purple region) are clearly marked. When we zoom in to study the vertical distribution of Cu, Sn, Zn, and S (Figure 2b), impressively, all four elements are quite uniform through the whole depth of the vertically aligned TNR array. The calculated elemental ratio from XPS high-resolution spectra seems to be near stoichiometric in this case; however, we should keep in mind that it would be a very challenging task to trace the exact ratio of Cu/Zn/Sn/S given their low signal level.

So far we have confirmed the presence of all constituent elements and verified that all Cu, Zn, Sn, and S have distributed inside the film made of TNR. Further, as for crystalline CZTS phase identification, Raman spectroscopy is by-far the most common and effective way.[23−25] Figure 3 shows the Raman spectra of the TNR@CZTS film obtained with 785 nm laser to provide a high-resolution image. Comparing the spectra, before and after CZTS deposition in Figure 3b, the only significant difference is seen at the small wavenumber range (250−400 $cm^{-1}$), where the crystalline CZTS characteristic peak clearly shows up. Further, to better evaluate the quality of crystalline CZTS, the marked region was replotted in Figure 3a together with the Lorentzian curve fitted peaks to identify different Raman modes. The dominating peak centered at 338 $cm^{-1}$ is attributed to the main A mode of CZTS; further there is a slightly left-shifted one at 332 $cm^{-1}$ broadening the main peak, which usually represents the degree of Cu/Zn disorder.[26] The peak centered at 287 $cm^{-1}$ corresponds to the second A mode of CZTS and 367 and 376 $cm^{-1}$ belong to E and B modes, respectively. Other less significant peaks identified from the fitted curves also agree with previous findings.[27] Besides, in previous research, the intensity ratio of the peaks centered at 287−303 $cm^{-1}$ ($I_{287}/I_{303}$) and 332−338 $cm^{-1}$ ($I_{332}/I_{338}$) were investigated as indicators for the degree of Cu/Zn disorder,[26,28] that is, the quality of crystalline CZTS. According to the fitting results, $I_{287}/I_{303}$ is 2.45 while $I_{332}/I_{338}$ is 0.15 for our in situ formed CZTS crystallites on TNR; these values are comparable to those of highly ordered kesterite reported by Scragg et al. and Caballero et al., again serving to confirm the very good quality of the crystalline CZTS.

So far, we have successfully proven the deposition of CZTS crystallites and studied its spatial distribution within the TNR scaffold. However, we have not yet got any evidence of CZTS with SEM but only the rutile substrate, which makes us think that CZTS is in the form of very tiny crystallites bonded onto the TNRs. In order to substantiate this supposition, the TNR@CZTS heterostructure was examined by transmission electron microscopy (TEM). The obtained TEM images show (refer to Figure 4) the composite material to consist of $TiO_2$ nanorods of different sizes that are decorated with very fine nanocrystallites. Figure 4a−c shows the bright field TEM images of three typical types of CZTS decorated nanorods scraped from the TNR@CZTS film, and Figure 4d−f depicts their corresponding high-angle annular dark-field images (HAADF) under scanning transmission electron microscope (STEM) working mode. The length of these three rods varied from ∼100 nm to ∼500 nm to ∼1 μm while their widths increased from ∼20 nm to ∼50 nm to ∼150 nm, respectively. In Figure

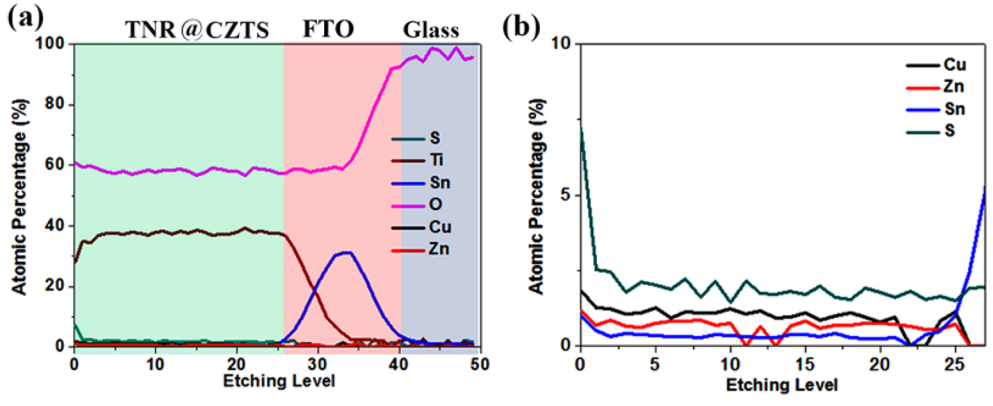


**Figure 2.** (a) XPS depth profile of all elements and (b) the "zoom in" view of the CZTS elements of the TNR@CZTS region (Ti and O excluded).


DOI: 10.1021/acsami.5b05732
ACS Appl. Mater. Interfaces 2015, 7, 22888−22897

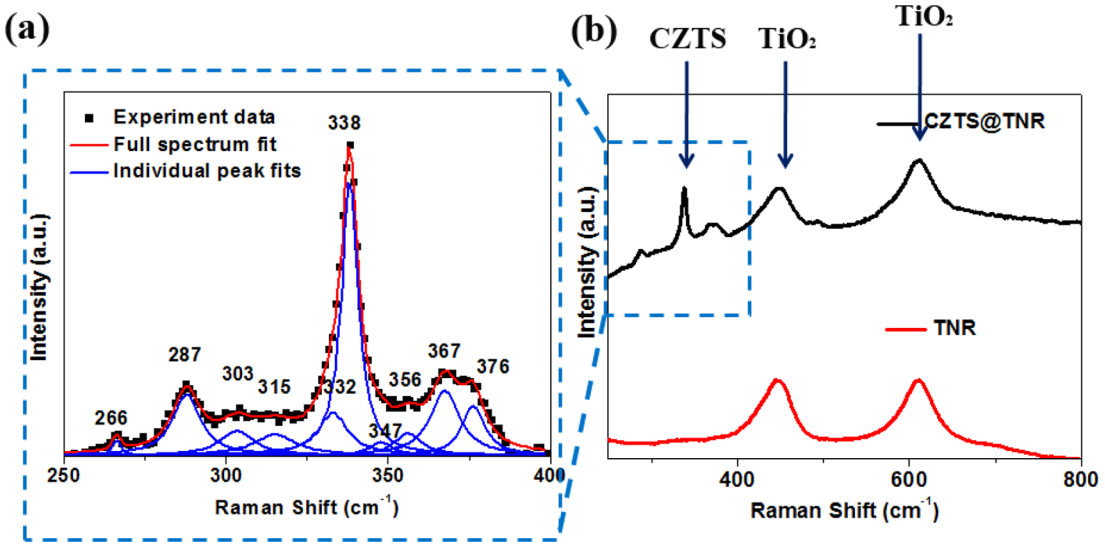


**Figure 3.** (a) Raman spectrum in the small wavenumber range with fitted peaks and (b) the overall spectrum of TNR@CZTS (black line) compared to that of pure TNR.

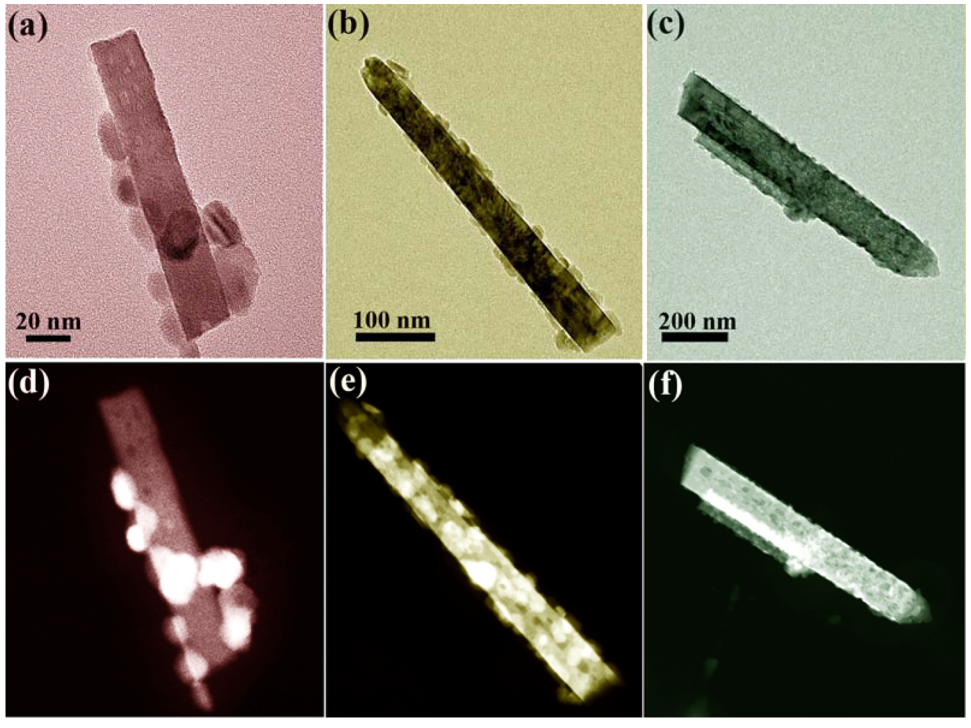


**Figure 4.** (a–c) Bright field TEM images of three different TNR@CZTS decorated nanorods with varied sizes and (d–f) their corresponding STEM-HAADF images.

4c, the CZTS nanocrystallites are not quite visible due to their significantly smaller size (10–20 nm) in comparison to the other nanorod specimens. More interestingly, in Figure 4c, there is a smaller rod attached to the larger one, which is of the same length as that in Figure 4b. This is a fortunate evidence that the ultrafine decorated bar is indeed the subunit from which the film is constructed. As HAADF-STEM forms the annular dark field image only by very high angle, incoherently scattered electrons are highly sensitive to variations in the atomic number of atoms (Z-contrast images) allowing to distinguish between $TiO_2$ and $Cu_2ZnSnS_4$ phases. This allows us to obtain a good knowledge of how these two phases are distributed, as $Cu_2ZnSnS_4$ has much higher overall atomic number than $TiO_2$. In the lower half of Figure 4, especially in parts d and e, the deposited nanoparticles can be seen to have contrasting brightness vis-à-vis the nanorods that clearly suggest that they are CZTS while the bar is rutile.

To confirm the formation of CZTS on the $TiO_2$ nanorods, herein we collected EDS maps from the bar shown in Figure 4f. A small area was selected (red dashed line marked area in Figure 5a) where a few bright particles could be seen attached on the big nanorod. From the mapping results in Figure 5d, the phase distribution can be inferred. $TiO_2$ constitutes the bulk area while Cu, Zn, Sn, and S are clearly concentrated on the edge, as evident by the higher brightness of HAADF-STEM. In order to ensure that the same configuration exists throughout


DOI: 10.1021/acsami.5b05732
ACS Appl. Mater. Interfaces 2015, 7, 22888–22897

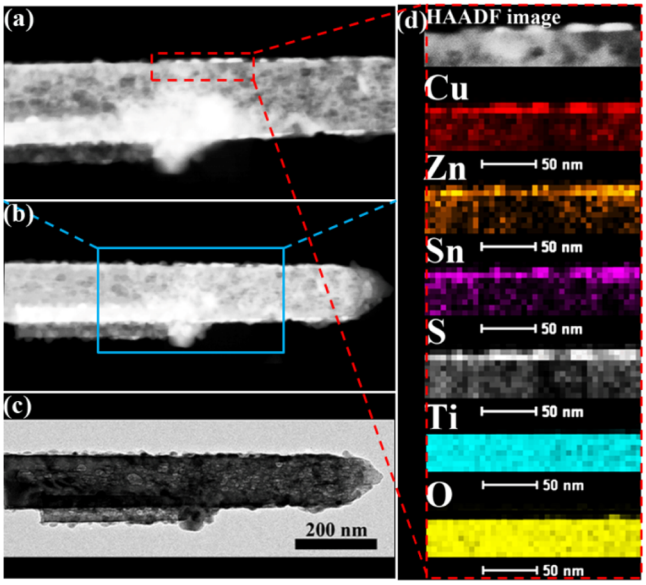


**Figure 5.** (a,b) STEM-HAADF and (c) bright field TEM image of the TNR@CZTS nanostructure and (d) magnified STEM-HAADF image of the rectangular dashed line area with the corresponding EDS element maps.

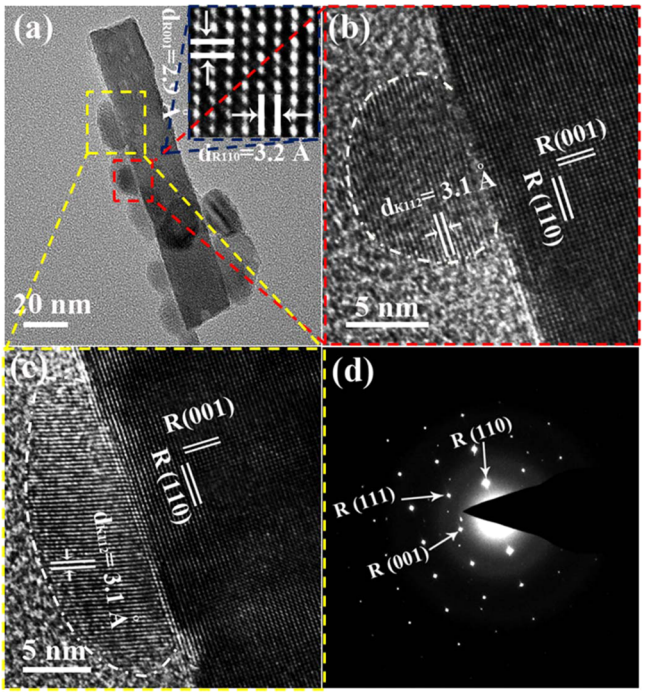


**Figure 6.** (a) Bright field TEM image of CZTS nanoparticles on a single rutile $TiO_2$ nanorod; the inset shows a magnified high-resolution image of the mark area on TNR; (b,c) HRTEM images of the TNR@CZTS structure with marked interplanar distance; (d) corresponding SAED pattern (K represents kesterite CZTS phase and R rutile $TiO_2$).

the TNR@CZTS film, we mapped the whole nanocomposite bar and found similar results as shown in Figure S4, thus supporting our conclusion.

So far we have verified the CZTS nanoparticle-decorated $TiO_2$ nanorod structure. Next we further investigated the detailed features of the CZTS@$TiO_2$ structure by performing high-resolution TEM imaging (HRTEM) on the smallest decorated nanorod (Figure 6a). In the inset, the magnified HRTEM image of the marked area, with lattice fringes at $d_{R110} \approx 3.2$ Å and $d_{R001} \approx 2.9$ Å interplanar spacings, is consistent with the rutile-$TiO_2$ phase.[6,19] HRTEM images of the boundary areas, where CZTS nanocrystallites and $TiO_2$ nanorod coexisted, were taken and shown in Figure 6b,c. The dominant kesterite CZTS (112) interplanar distance in both cases was determined to be ~3.1 Å, which is slightly smaller than that of rutile (110) as reported by previous researchers.[29,30] The CZTS nanocrystallites attached to the nanorod are of different shape as seen in Figure 6b,c and their average size was estimated to be approximately 5−20 nm. One noteworthy point here is the good bonding/interfacing between CZTS and $TiO_2$. Such in situ epitaxial-like growth is advantageous in allowing the photoelectrons generated from CZTS to be efficiently injected to $TiO_2$ with less recombination occurrence. A selected area electron diffraction (SAED) image was also taken for this small region in Figure 6d. The sharp diffraction pattern clearly indicates the nanorod to be single crystal rutile; at the same time there are several isolated dots that are attributed to the small CZTS crystallites. Two additional low-magnification TEM images of the larger TNR@CZTS heterostructures are provided in Figure S5a,c together with their corresponding SAED patterns in Figure S5b,d. In this instance, since there are more CZTS crystallites decorating the bigger rutile rod, instead of having randomly located isolated dots, we can observe a ring-like diffraction pattern formed close to the strong diffractive R(110) plane, which is much likely due to differently oriented kesterite (112) plane.

After having successfully built this TNR@CZTS heterostructure, it is important to prove its functionality; in other words, to answer the question whether the photoelectrons generated from the CZTS nanocrystalline light absorber can "hop" to the nanorod carrier conductor before being recombined. Incident photon-to-current efficiency (IPCE) that quantifies the percentage of photons being converted into finally collected electrons at different photon energies could reveal indeed the visible-light-driven photon-electron conversion performance. To measure the optoelectronic performance, we simply employed the "sandwich" photoelectrochemical cell configuration with Pt as the counter electrode and $I^-/I_3^-$ as the hole conductor-electrolyte.[20] Results are shown in Figure 7a. To eliminate the interference of TNR itself, which is ultraviolet photosensitive, the pure TNR electrode was also studied and a significant difference in the visible region (colored in blue) was noticed. This difference perfectly confirms the effectiveness of the deposited CZTS nanocrystallites as a visible light absorber. The quantum efficiency cutoff of this TNR@CZTS photoanode is at around 800 nm, which is consistent with the reported 1.5 eV bandgap of kesterite-CZTS. Unfortunately, the external quantum efficiency (EQE) is relatively low compared to the well-studied CZTS thin film solar cells,[31] only ~12% at the blue light region. The external quantum efficiency is governed by three factors: the light harvesting efficiency ($\eta_{lh}$), the charge injection efficiency ($\eta_{inj}$), and the charge collection efficiency ($\eta_{cc}$). The relation among them is expressed by

$$\eta_{IPCE} = \eta_{lh}\eta_{inj}\eta_{cc}$$

One possible reason for the low EQE value could be due to optical loss. To evaluate the effect of this factor, we measured the optical transmittance (Figure S6a) and reflectance (Figure S6b) for both TNR films before and after CZTS deposition and


DOI: 10.1021/acsami.5b05732
ACS Appl. Mater. Interfaces 2015, 7, 22888−22897

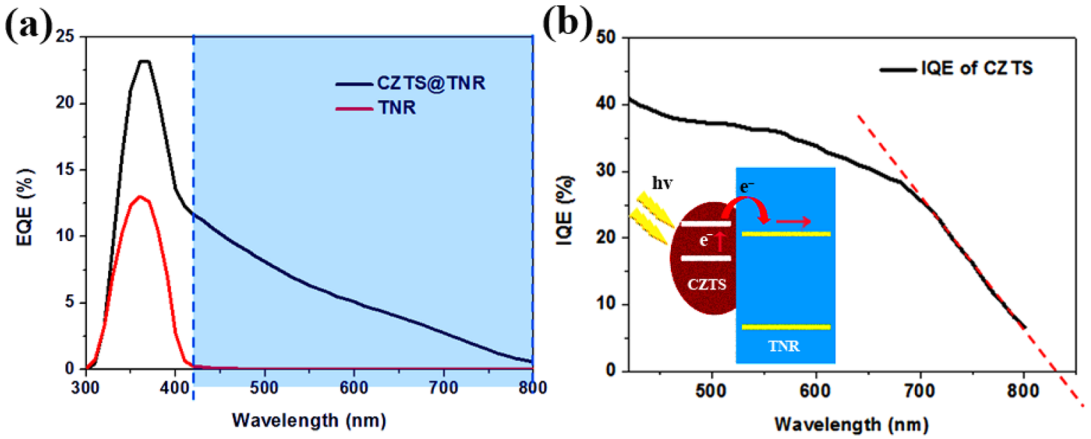


**Figure 7.** (a) IPCE of devices with TNR@CZTS photoanode compared to that with only TNR and (b) calculated internal quantum efficiency of CZTS in the visible range.

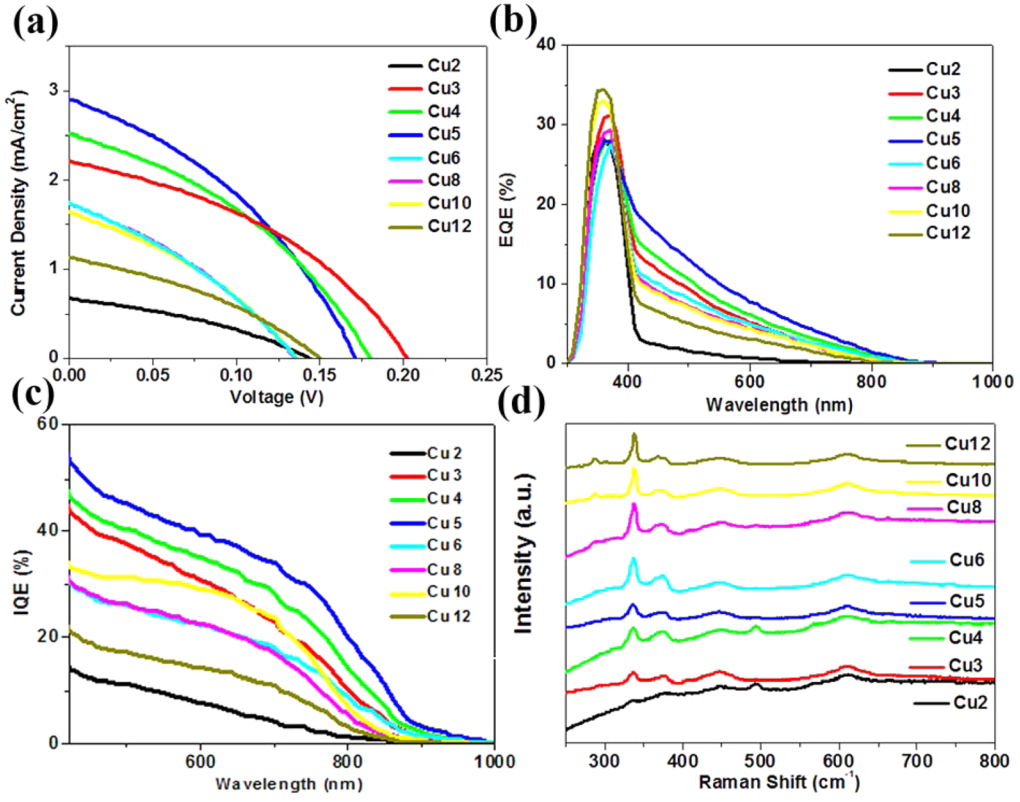


**Figure 8.** (a) *J*–*V* curves, (b) external quantum efficiency, and (c) calculated internal quantum efficiency of ETA devices based on TNR@CZTS photoanodes prepared with different CuS SILAR deposition cycles, and (d) Raman spectra of the respective photoanodes.

then calculated the true light absorption ($A$) of the isolated CZTS nanomaterial alone by adding up the reduced portion of reflection ($R$) and transmittance ($T$) after CZTS deposition:

$$A_{CZTS} = (T_{TNR} - T_{TNR@CZTS}) + (R_{TNR} - R_{TNR@CZTS})$$

In Figure S6c, the blue region under the plot demonstrates that less than 20% of illumination in the visible region contributes to photon-electron conversion. This prompted us to further probe the optoelectronic property of CZTS nanocrystallites by calculating its internal quantum efficiency in the visible region. The result shown in Figure 7b indicates a value of nearly 40% in the blue light region. This means that if we could manage to reduce the optical loss of the photoanode, it would be possible to significantly increase the device photocurrent. We did a linear fit of the efficiency curve edge and found the cutoff wavelength to be around 830 nm, which corresponds to a bandgap of approximately 1.49 eV, perfectly matching the theoretical semiconductor characteristic of kesterite-CZTS.[32,33] However, this IQE value is still low compared to thin-film kesterite PV devices. This could be attributed to inefficient charge injection ($\eta_{inj}$) and/or collection ($\eta_{cc}$). For successful injection good band alignment is a prerequisite, namely, the conduction band bottom of the absorber should be above that of the electron conductor to supply sufficient injection overpotential.[17] Since the photogenerated electrons were successfully collected, it is implied the interfacial energy band alignment to be as shown in the inset of


DOI: 10.1021/acsami.5b05732
ACS Appl. Mater. Interfaces 2015, 7, 22888−22897

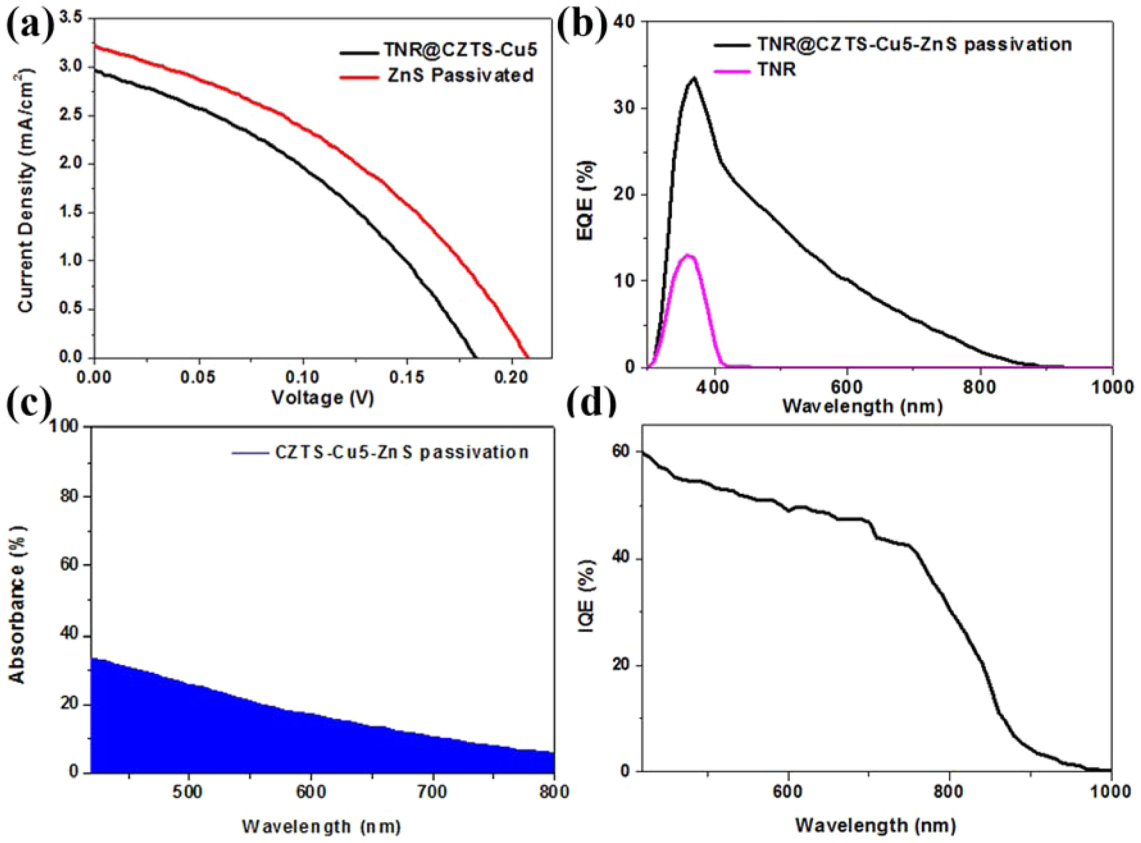


**Figure 9.** (a) $J-V$ curves, (b) external quantum efficiency, (c) measured light absorption, and (d) calculated internal quantum efficiency of ETA cells based on TNR@CZTS photoanodes prepared with 5 CuS SILAR deposition cycles and passivated with ZnS.

Figure 7b, proving thus the photovoltaic activity of the TNR@CZTS nanostructure. Hence the competition between injection/collection and recombination play a vital role in device performance that needs to be controlled for optimum results. The $J-V$ characteristic curves shown in Figure S7 reveal a higher short circuit current density of 1.65 mA/cm$^2$ than previously reported values with CZTS sensitized solar cell structures by Wang et al.[15] (0.71 mA/cm$^2$) and by Dai et al.[16] (0.36−0.71 mA/cm$^2$). The better contact due to the in situ epitaxial-like growth of CZTS on TNR and the one-dimensional electron conductor with shorter electron pathway are responsible for the increased current.

However, the $V_{oc}$ is only 0.16 V, which is much lower than the original TNR photoanode-based device, causing a poor efficiency of only 0.1%. To understand the origin of the abnormally low open circuit voltage after CZTS deposition, we performed XPS on the TNR alone on FTO glass as well as the TNR@CZTS electrode and found a ∼0.2 eV down shift of the Ti $2p_{2/3}$ spectrum after CZTS deposition, refer to Figure S8a. To validate the accuracy of the measurement, we prepared several photoanodes carefully following the same synthesis routine and we made their measurements at the same time on the same equipment, with the C 1s peak set to 285.00 eV for charge correction; the down shift value was found always to be between 0.19 and 0.23 eV. This downshift indicates a decrease of the Fermi energy after CZTS deposition as shown in Figure S8b.[34] Since the maximum open circuit voltage is determined by the difference between the Fermi level of semiconductor and the electrochemical potential of electrolyte under illumination as shown in Figure S9,[35] this downshift could induce a certain decrease of max $V_{oc}$ compared to pure rutile photoanode-based photoelectrochemical cell. Meanwhile, interfacial recombination could have also caused additional decline in the photovoltage.

To improve the device optoelectronic performance further work focusing on controlling the CZTS deposit properties was pursued. This was done by varying the cycles of copper sulfide deposition from 2 to 12 times (Cu2 ∼ Cu12 for short) during SILAR 1, while other conditions remained unchanged. This round of investigation revealed a strong dependency of photoelectrochemical response on CuS deposition cycles as can be seen in Figure 8. In Figure 8a, 5 SILAR cycles of Cu predeposition leads to the highest $J_{sc}$ of around 3 mA/cm$^2$, almost doubling the previous value. EQE and IQE curves in Figure 8b,c reveal ∼20% and ∼50% external and internal quantum efficiency at the blue light region for the champion device, respectively. As a complex material, optimization of CZTS as an inorganic sensitizer is not straightforward meaning that there is a lot of work to be done toward achieving competitive solar cell efficiency level. However, the observed improvement via alternation of SILAR cycle numbers serves to show that device optimization can prove very fruitful. To understand the effect of CuS SILAR deposition cycle on CZTS quality, Raman spectroscopy was performed with 785 nm laser. The intensity of CZTS characteristic peak at ∼337 cm$^{-1}$ was found to keep increasing with the number of Cu SILAR deposition cycles (Figure 8d) apparently due to CZTS crystallite size growth,[36,37] and the probably varied composition of CZTS with different initial copper ratios may also cause the profile changes of the Raman spectra. According to the


DOI: 10.1021/acsami.5b05732
ACS Appl. Mater. Interfaces 2015, 7, 22888−22897

photoelectrochemical device performance among the different SILAR deposited photoanodes, the Cu5 yields the best relatively results. To understand the reason for the enhancement of performance, we applied ICP-OES to obtain more accurate compositional information by dissolving those CZTS crystallites (after HCl treatment) in aqua regia. The results presented in Figure S10 show great variations of the Cu/Sn/Zn ratio with a Cu5 sample suggesting a copper-poor zinc-rich near-stoichiometric composition, which is generally accepted to have a better electronic property[3] over other compositions. However, the reason for the observed trend having copper percentage first decreasing and then rising as the number of initial copper SILAR cycles increases while zinc behaves the opposite way is unclear. We hypothesize that the amount of copper sulfides initially deposited on TNR could be critical to the nucleation pathways of the following deposited SnS and ZnS impacting the reactive crystallization of CZTS upon annealing. Further work is underway seeking to optimize the composition, morphology, and optical properties of the CZTS nanocrystallites grown on TNR.

While the varied precursor deposition procedure led to photocurrent output increase, the $V_{oc}$ remained still low at ~0.2 V. Surface passivation with metal oxides (i.e., $Al_2O_3$, $ZrO_2$) or metal chalcogenides (i.e., CdSe, ZnS) have proven in the past to effectively reduce interfacial recombination and hence increase photovoltage in the case of quantum-dot sensitized solar cells and other extremely thin absorber solar cells.[17] This approach was also tested in this work after first treating the TNR@CZTS photoanodes with a strong HCl acid solution (4 M) to remove acid-soluble impurities.[38] To this end, two additional SILAR cycles were applied to deposit extra ZnS similar to the SILAR 3 step. The $J-V$ curves for the best performed Cu5 device before and after ZnS treatment are shown in Figure 9a. It is clear that the surface passivation had a measurable effect in rising both the $J_{sc}$ and $V_{oc}$ to 3.22 mA/cm$^2$ and 0.21 V, respectively; hence, the overall efficiency is improved from 0.2% to 0.25%. The highest external and internal quantum efficiencies at the blue light region are ~22% and ~60%, respectively. Although the improvement is modest, this result indicates a feasible direction for further performance improvement. According to recent progress in quantum-dot sensitized solar cells reported by Zhao et al.,[39] their efficiency increased more than 3 times after an optimized ZnS/$SiO_2$ passivation treatment applied to control severe interfacial recombination arising from surface defect states. For semiconductor nanocrystals with quaternary composition like CZTS the problem of surface defects, inhomogeneity, and impurities is deemed to be even more prevalent in comparison to binary metal chalcogenides; hence, the pursuing in future work of optimized surface passivation approaches is of great importance in further boosting its IQE. Meanwhile, when evaluating the light absorption by CZTS (compare Figure 9c to Figure S6c), neither the number of copper sulfide SILAR cycles during precursor preparation nor the application of ZnS passivating film are seen to have a measurable effect on the light harvesting capacity of TNR@CZTS photoanodes. Still less than a quarter of visible light energy contributes to the photon-electron conversion. This implies that the amount of CZTS nanocrystal loading should be increased and on the other hand interfacial recombination suppressed, a strategy that we pursue via the growth of denser CZTS nanocrystallites on longer rutile nanorods capped with a continuous CZTS film properly passivated.

A certain amount of sodium has been reported to improve the performance of CZTS solar cells;[40] however, too much sodium could become an issue. Since our experiment involved deposition from sodium sulfide solution, we checked the sodium content in our TNR@CZTS photoelectrode and the data is shown in Figure S11. The XPS depth profile of the Cu5 TNR@CZTS (without additional ZnS layer) did reveal a significant amount of sodium to be present in the film (more than 5%). The excess sodium could have contributed to some extent to the low $V_{oc}$ exhibited by the photoanode, an issue that deserves further investigation. Similarly the presence and potential interference of minor binaries like copper sulfides or tin sulfides need to be further probed as part of future investigations. Furthermore, because the stability of CZTS in contact with the $I^-/I_3^-$ electrolyte is an open question, the present device as tested is considered as a "half-cell" useful only in demonstrating the activity of TNR@CZTS in visible-light-driven photoelectron generation. In order to fully realize its potential, a suitable electrolyte is needed on one hand to stabilize the inorganic photoanode and on the other hand to more efficiently extract positive charges from CZTS. The widely used polysulfide electrolyte in quantum-dot sensitized solar cell research would be a good choice, which could allow us having more choices of passivation layers, CdS, for example, is unstable in the $I^-/I_3^-$ electrolyte but can be used as a buffer layer in the polysulfide system.[41] Alternatively, solid state hole transport materials (HTM) with higher stability (like CuSCN) could replace the liquid electrolyte.[17] In summary, further work focusing on interfacial TNR@CZTS/HTM engineering should be pursued for minimizing the downshift of Fermi level and reducing recombination, so as to fully unlock the optoelectronic device potential of the CZTS extremely thin absorber solar cell.

## CONCLUSION

We have developed a SILAR-controlled method to in situ deposit, following annealing in S vapor atmosphere, quaternary semiconductor $Cu_2ZnSnS_4$ nanocrystallites of uniform composition on rutile-$TiO_2$ nanorod array films of ~1.5 $\mu$m thickness. The nanoengineered TNR@CZTS photoanode structure consists of 5–20 nm kesterite-CZTS nanocrystallites well bonded on rutile nanorods with variable sizes. Then we have demonstrated the feasibility of generating and injecting photoelectrons from CZTS to the closely attached $TiO_2$ nanorods. Further we demonstrated that by adjusting the number of CuS SILAR cycles, the growth of CZTS nanocrystallites can be controlled for improved photocurrent response. Finally surface passivation with ZnS is shown to be partly effective in suppressing interfacial recombination yielding a short circuit current density of 3.22 mA/cm$^2$ corresponding to an internal quantum efficiency of ~60% in the blue light region. However, the open circuit voltage is only 0.21 V, which is concluded to be due to the down shift of Fermi level of $TiO_2$ after CZTS deposition as well as incomplete suppression of interfacial recombination and instability introduced by the $I^-/I_3^-$ electrolyte. We believe that this new extremely thin absorber CZTS-conductor TNR configuration via further optimization of the TNR@CZTS/HTM interface has the potential for enabling the development of environmentally friendly and low-cost photovoltaic devices made of abundant materials.


DOI: 10.1021/acsami.5b05732
ACS Appl. Mater. Interfaces 2015, 7, 22888–22897

## ■ ASSOCIATED CONTENT

### Supporting Information

The Supporting Information is available free of charge on the ACS Publications website at DOI: 10.1021/acsami.5b05732.

Schematic processes for the in situ deposition of CZTS; XPS spectra; TEM bright field images, HAADF-STEM images and EDS maps; optical properties including transmittance, reflectance, calculated visible light absorption, and estimated bandgap; $J-V$ characteristic curves; energy band diagram of $TiO_2$/CZTS/electrolyte/CE system; metallic element ratio of CZTS; XPS depth profile of Cu5 sample (PDF)

## ■ AUTHOR INFORMATION


### Corresponding Author

*E-mail: george.demopoulos@mcgill.ca.


### Author Contributions

The work was conceived and designed by both authors; Z.W. performed all experiments. Analysis was done by Z.W. and assisted by G.P.D. The manuscript was written by Z.W. and corrected by G.P.D. The overall research was directed by G.P.D. Both authors have given approval to the final version of the manuscript.

### Notes

The authors declare no competing financial interest.

## ■ ACKNOWLEDGMENTS

This work was funded by the Natural Sciences & Engineering Research Council (NSERC) through a strategic project grant to G.P.D. and sponsored by Targray Technology International, 5N Plus, and CIS Scientific. The authors would like to thank Dr. Xuedong Liu for the assistance with TEM imaging and Dr. Samir Elouatik of Université de Montréal for assistance with the Raman Renishaw inVia Raman spectrometer.

## ■ REFERENCES


(1) Katagiri, H.; Jimbo, K.; Maw, W. S.; Oishi, K.; Yamazaki, M.; Araki, H.; Takeuchi, A. Development of CZTS-Based Thin Film Solar Cells. *Thin Solid Films* **2009**, *517*, 2455−2460.

(2) Lan, X.; Masala, S.; Sargent, E. H. Charge-Extraction Strategies for Colloidal Quantum Dot Photovoltaics. *Nat. Mater.* **2014**, *13*, 233−240.

(3) Wang, W.; Winkler, M. T.; Gunawan, O.; Gokmen, T.; Todorov, T. K.; Zhu, Y.; Mitzi, D. B. Device Characteristics of CZTSSe Thin-Film Solar Cells with 12.6% Efficiency. *Adv. Energy Mater.* **2014**, *4*, 1301465.

(4) Cho, J. W.; Ismail, A.; Park, S. J.; Kim, W.; Yoon, S.; Min, B. K. Synthesis of $Cu_2ZnSnS_4$ Thin Films by a Precursor Solution Paste for Thin Film Solar Cell Applications. *ACS Appl. Mater. Interfaces* **2013**, *5*, 4162−4165.

(5) Wang, G.; Zhao, W.; Cui, Y.; Tian, Q.; Gao, S.; Huang, L.; Pan, D. Fabrication of a $Cu_2ZnSn(S,Se)_4$ Photovoltaic Device by a Low-Toxicity Ethanol Solution Process. *ACS Appl. Mater. Interfaces* **2013**, *5*, 10042−10047.

(6) Wang, Z.; Wang, H.; Liu, B.; Qiu, W.; Zhang, J.; Ran, S.; Huang, H.; Xu, J.; Han, H.; Chen, D.; Shen, G. Transferable and Flexible Nanorod-Assembled $TiO_2$ Cloths for Dye-Sensitized Solar Cells, Photodetectors, and Photocatalysts. *ACS Nano* **2011**, *5*, 8412−8419.

(7) Jeon, I. Y.; Kim, H. M.; Choi, I. T.; Lim, K.; Ko, J.; Kim, J. C.; Choi, H. J.; Ju, M. J.; Lee, J. J.; Kim, H. K.; Baek, J.-B. High-Performance Dye-Sensitized Solar Cells Using Edge-Halogenated Graphene Nanoplatelets as Counter Electrodes. *Nano Energy* **2015**, *13*, 336−345.

(8) Zhang, Y.; Diao, Y.; Lee, H.; Mirabito, T. J.; Johnson, R. W.; Puodziukynaite, E.; John, J.; Carter, K. R.; Emrick, T.; Mannsfeld, S. C. B.; Briseno, A. L. Intrinsic and Extrinsic Parameters for Controlling the Growth of Organic Single-Crystalline Nanopillars in Photovoltaics. *Nano Lett.* **2014**, *14*, 5547−5554.

(9) Li, H.; Cao, J.; Zhou, Q.; Ding, L.; Wang, J. High-Performance Inverted PThTPTI:PC71BM Solar Cells. *Nano Energy* **2015**, *15*, 125−134.

(10) Im, J.-H.; Luo, J.; Franckevičius, M.; Pellet, N.; Gao, P.; Moehl, T.; Zakeeruddin, S. M.; Nazeeruddin, M. K.; Grätzel, M.; Park, N. G. Nanowire Perovskite Solar Cell. *Nano Lett.* **2015**, *15*, 2120−2126.

(11) Zhong, D.; Cai, B.; Wang, X.; Yang, Z.; Xing, Y.; Miao, S.; Zhang, W. H.; Li, C. Synthesis of Oriented $TiO_2$ Nanocones with Fast Charge Transfer for Perovskite Solar Cells. *Nano Energy* **2015**, *11*, 409−418.

(12) Selinsky, R. S.; Ding, Q.; Faber, M. S.; Wright, J. C.; Jin, S. Quantum Dot Nanoscale Heterostructures for Solar Energy Conversion. *Chem. Soc. Rev.* **2013**, *42*, 2963−2985.

(13) Sinsermsuksakul, P.; Sun, L.; Lee, S. W.; Park, H. H.; Kim, S. B.; Yang, C.; Gordon, R. G. Overcoming Efficiency Limitations of SnS-Based Solar Cells. *Adv. Energy Mater.* **2014**, *4*, 1400496.

(14) Page, M.; Niitsoo, O.; Itzhaik, Y.; Cahen, D.; Hodes, G. Copper Sulfide as a Light Absorber in Wet-Chemical Synthesized Extremely Thin Absorber (ETA) Solar Cells. *Energy Environ. Sci.* **2009**, *2*, 220−223.

(15) Wang, Y.; Li, C. X.; Yin, X. J.; Wang, H.; Gong, H. $Cu_2ZnSnS_4$ (CZTS) Application in $TiO_2$ Solar Cell as Dye. *ECS J. Solid State Sci. Technol.* **2013**, *2*, Q95−Q98.

(16) Dai, P.; Shen, X.; Lin, Z.; Feng, Z.; Xu, H.; Zhan, J. Band-Gap Tunable $(Cu_2Sn)_{x/3}Zn_{1-x}S$ Nanoparticles for Solar Cells. *Chem. Commun.* **2010**, *46*, 5749−5751.

(17) Roelofs, K. E.; Brennan, T. P.; Bent, S. F. Interface Engineering in Inorganic-Absorber Nanostructured Solar Cells. *J. Phys. Chem. Lett.* **2014**, *5*, 348−360.

(18) Hodes, G.; Cahen, D. All-Solid-State, Semiconductor-Sensitized Nanoporous Solar Cells. *Acc. Chem. Res.* **2012**, *45*, 705−713.

(19) Liu, B.; Aydil, E. S. Growth of Oriented Single-Crystalline Rutile $TiO_2$ Nanorods on Transparent Conducting Substrates for Dye-Sensitized Solar Cells. *J. Am. Chem. Soc.* **2009**, *131*, 3985−3990.

(20) Wang, Z.; Ran, S.; Liu, B.; Chen, D.; Shen, G. Multilayer $TiO_2$ Nanorod Cloth/Nanorod Array Electrode for Dye-Sensitized Solar Cells and Self-Powered UV Detectors. *Nanoscale* **2012**, *4*, 3350−3358.

(21) Yan, P.; Wang, X.; Zheng, X.; Li, R.; Han, J.; Shi, J.; Li, A.; Gan, Y.; Li, C. Photovoltaic Device Based on $TiO_2$ Rutile/Anatase Phase Junctions Fabricated in Coaxial Nanorod Arrays. *Nano Energy* **2015**, *15*, 406−412.

(22) Ho, T. Y.; Chen, L. Y. The Study of $Cu_2ZnSnS_4$ Nanocrystal/$TiO_2$ Nanorod Heterojuction Photoelectrochemical Cell for Hydrogen Generation. *Energy Procedia* **2014**, *61*, 2050−2053.

(23) Lin, X.; Kavalakkatt, J.; Kornhuber, K.; Levcenko, S.; Lux-Steiner, M. C.; Ennaoui, A. Structural and Optical Properties of $Cu_2ZnSnS_4$ Thin Film Absorbers from ZnS and $Cu_3SnS_4$ Nanoparticle Precursors. *Thin Solid Films* **2013**, *535*, 10−13.

(24) Berg, D. M.; Djemour, R.; Gütay, L.; Siebentritt, S.; Dale, P. J.; Fontane, X.; Izquierdo-Roca, V.; Pérez-Rodriguez. Raman Analysis of Monoclinic $Cu_2SnS_3$ Thin Films. A. *Appl. Phys. Lett.* **2012**, *100*, 192103.

(25) Fontané, X.; Calvo-Barrio, L.; Izquierdo-Roca, V.; Saucedo, E.; Pérez-Rodriguez, A.; Morante, J. R.; Berg, D. M.; Dale, P. J.; Siebentritt, S. In-Depth Resolved Raman Scattering Analysis for the Identification of Secondary Phases: Characterization of $Cu_2ZnSnS_4$ Layers for Solar Cell Applications. *Appl. Phys. Lett.* **2011**, *98*, 181905.

(26) Scragg, J. J. S.; Choubrac, L.; Lafond, A.; Ericson, T.; Platzer-Björkman, C. A Low-Temperature Order-Disorder Transition in $Cu_2ZnSnS_4$ Thin Films. *Appl. Phys. Lett.* **2014**, *104*, 041911.

(27) Dimitrievska, M.; Fairbrother, A.; Fontané, X.; Jawhari, T.; Izquierdo-Roca, V.; Saucedo, E.; Pérez-Rodríguez, A. Multiwavelength Excitation Raman Scattering Study of Polycrystalline Kesterite $Cu_2ZnSnS_4$ Thin Films. *Appl. Phys. Lett.* **2014**, *104*, 021901.




DOI: 10.1021/acsami.5b05732
*ACS Appl. Mater. Interfaces* 2015, 7, 22888−22897

(28) Caballero, R.; Garcia-Llamas, E.; Merino, J. M.; León, M.; Babichuk, I.; Dzhagan, V.; Strelchuk, V.; Valakh, M. Non-Stoichiometry Effect and Disorder in $Cu_2ZnSnS_4$ Thin Films Obtained by Flash Evaporation: Raman Scattering Investigation. *Acta Mater.* **2014**, *65*, 412−417.
(29) Liu, W. C.; Guo, B. L.; Wu, X. S.; Zhang, F. M.; Mak, C. L.; Wong, K. H. Facile Hydrothermal Synthesis of Hydrotropic $Cu_2ZnSnS_4$ Nanocrystal Quantum Dots: Band-Gap Engineering and Phonon Confinement Effect. *J. Mater. Chem. A* **2013**, *1*, 3182−3186.
(30) Steinhagen, C.; Panthani, M. G.; Akhavan, V.; Goodfellow, B.; Koo, B.; Korgel, B. A. Synthesis of $Cu_2ZnSnS_4$ Nanocrystals for Use in Low-Cost Photovoltaics. *J. Am. Chem. Soc.* **2009**, *131*, 12554−12555.
(31) Shin, B.; Gunawan, O.; Zhu, Y.; Bojarczuk, N. A.; Chey, S. J.; Guha, S. Thin Film Solar Cell with 8.4% Power Conversion Efficiency Using an Earth-Abundant $Cu_2ZnSnS_4$ Absorber. *Prog. Photovoltaics* **2013**, *21*, 72−76.
(32) Katagiri, H.; Saitoh, K.; Washio, T.; Shinohara, H.; Kurumadani, T.; Miyajima, S. Development of Thin Film Solar Cell Based on $Cu_2ZnSnS_4$ Thin Films. *Sol. Energy Mater. Sol. Cells* **2001**, *65*, 141−148.
(33) Ichimura, M.; Nakashima, Y. Analysis of Atomic and Electronic Structures of $Cu_2ZnSnS_4$ Based on First-Principle Calculation. *Jpn. J. Appl. Phys.* **2009**, *48*, 090202.
(34) Scanlon, D. O.; Dunnill, C. W.; Buckeridge, J.; Shevlin, S. A.; Logsdail, A. J.; Woodley, S. M.; Catlow, C. R. A.; Powell, M. J.; Palgrave, R. G.; Parkin, I. P.; Watson, G. W.; Keal, T. W.; Sherwood, P.; Walsh, A.; Sokol, A. A. Band Alignment of Rutile and Anatase $TiO_2$. *Nat. Mater.* **2013**, *12*, 798−801.
(35) O'Regan, B.; Gratzel, M. A Low-Cost, High-Efficiency Solar Cell Based on Dye-Sensitized Colloidal $TiO_2$ Films. *Nature* **1991**, *353*, 737−740.
(36) Becker, M. A.; Radich, J. G.; Bunker, B. A.; Kamat, P. V. How Does a SILAR CdSe Film Grow? Tuning the Deposition Steps to Suppress Interfacial Charge Recombination in Solar Cells. *J. Phys. Chem. Lett.* **2014**, *5*, 1575−1582.
(37) Li, B. J.; Yin, P. F.; Zhou, Y. Z.; Gao, Z. M.; Ling, T.; Du, X. W. Single Crystalline $Cu_2ZnSnS_4$ Nanosheet Arrays for Efficient Photochemical Hydrogen Generation. *RSC Adv.* **2015**, *5*, 2543−2549.
(38) Fairbrother, A.; García-Hemme, E.; Izquierdo-Roca, V.; Fontané, X.; Pulgarín-Agudelo, F. A.; Vigil-Galán, O.; Pérez-Rodríguez, A.; Saucedo, E. Development of a Selective Chemical Etch to Improve the Conversion Efficiency of Zn-Rich $Cu_2ZnSnS_4$ Solar Cells. *J. Am. Chem. Soc.* **2012**, *134*, 8018−8021.
(39) Zhao, K.; Pan, Z.; Mora-Seró, I.; Cánovas, E.; Wang, H.; Song, Y.; Gong, X.; Wang, J.; Bonn, M.; Bisquert, J.; Zhong, X. Boosting Power Conversion Efficiencies of Quantum-Dot-Sensitized Solar Cells Beyond 8% by Recombination Control. *J. Am. Chem. Soc.* **2015**, *137*, 5602−5609.
(40) Zhou, H.; Song, T. B.; Hsu, W. C.; Luo, S.; Ye, S.; Duan, H. S.; Hsu, C. J.; Yang, W.; Yang, Y. Rational Defect Passivation of $Cu_2ZnSn(S,Se)_4$ Photovoltaics with Solution-Processed $Cu_2ZnSnS_4$:Na Nanocrystals. *J. Am. Chem. Soc.* **2013**, *135*, 15998−16001.
(41) Lee, Y. L.; Chang, C. H.; Lee, Y. L.; Chang, C. H. Efficient Polysulfide Electrolyte for CdS Quantum Dot-Sensitized Solar Cells. *J. Power Sources* **2008**, *185*, 584−588.


DOI: 10.1021/acsami.5b05732
*ACS Appl. Mater. Interfaces* 2015, 7, 22888−22897